Electrochemical Dehydrogenation of Ethane to Ethylene in a Solid Oxide Electrolyser

Xirui Zhang[1], Lingting Ye[1], Hao Li[1], Fanglin Chen[2], Kui Xie[1,*]

[1] Key Laboratory of Design and Assembly of Functional Nanostructures, Fujian Institute of Research on the Structure of Matter, Chinese Academy of Sciences, Fuzhou, Fujian 350002, China.
[2] Department of Mechanical Engineering, University of South Carolina, 300 Main Street, Columbia, SC 29208, USA.
* Corresponding Author's E-mail: kxie@fjirsm.ac.cn

ABSTRACT: The conversion of ethane, a main component of natural gas, to ethylene feed stock has attracted widespread attentions since the worldwide shale gas revolution. Thermal catalysis of ethane to ethylene, mainly oxidative dehydrogenation, faces the fundamental challenge of low conversion, low selectivity and catalyst coking. This work demonstrates an efficient conversion of ethane to ethylene in a non-oxidative dehydrogenation process in a proton-conducting solid oxide electrolyser at ambient pressure and 700°C. We show the highest ethane conversion of 75.2% and ~100% ethylene selectivity even only at 0.8 V in this electrochemical catalysis process. The electrochemical pumping of protons at anode with active exsolved metal-oxide interfaces enhances anode activity while the metal-oxide interface interactions further engineer the ethane conversion in the electrochemical dehydrogenation process. We exsolve metal-oxide interface architecture at nanoscale on electrode scaffold to improve coking resistance and catalyst stability. We further present the reduction of carbon dioxide to carbon monoxide in the cathode combined with ethane conversion in the anode and we show the higher performance of ethane conversion in the anode with syngas production in the cathode. The electrochemical dehydrogenation process would provide an alternative method for the petrochemical production and a thermochemical practice in a clean energy mode.

KEYWORDS: *Solid oxide electrolysers; Electrochemical dehydrogenation; Metal-oxide interface; Ethane; Ethylene*

INTRODUCTION

Shale gas has demonstrated a huge potential to revolutionize the energy and chemical industry because of the recent increase in proven reserves. Ethylene (C_2H_4) is one of the basic components for the synthesis of chemical products in the chemical industry.[1,2] Because of the high fraction of ethane (C_2H_6) in shale gas (>20vol%), C_2H_6 has become a rich and economically attractive raw material for C_2H_4 production. Currently, steam cracking of tubular furnace is the main technology of C_2H_4 production, and ~99% of global C_2H_4 production uses the tubular furnace pyrolysis.[3,4] Typically, the steam cracking of C_2H_6 has a conversion rate of 70%, with C_2H_4 yields of about 50%. However, the steam cracking still face fundamental challenges including thermal constraints, operation at high temperatures, and energy-intensive process.

An alternative to steam cracking method is oxidative dehydrogenation (ODH) of C_2H_6 ($C_2H_6 + O_2 = 2C_2H_4 + 2H_2O$ and $C_2H_6 + CO_2 = C_2H_4 + CO + H_2O$). The ODH process can reduce carbon deposition from ethane splitting by lowering operation temperature,. There are reports of C_2H_4 yields of ~42% (750°C) and ~63% (850°C) with C_2H_4 selectivity up to ~90%.[5,6] However, the possible deep oxidation of hydrocarbons would reduce the C_2H_4 selectivity, and the mixture of C_2H_6 and O_2 is a potential safety hazard. In contrast, non-oxidative ethane dehydrogenation (EDH) avoids most ODH-related problems. EDH process is more attractive to the transformation of gas containing C_2H_6, such as shale field gas, refinery off-gas, shale gas in unfavorable geographical locations. The C_2H_6 conversion is ~28% and the C_2H_4 selectivity is about 70% at 600°C with ZSM-5 zeolite supported Fe catalysts. The shortcoming of EDH is that C_2H_4 and H_2 cannot be separated, which leads to low C_2H_6 conversion and C_2H_4 selectivity. Hence, if H_2 can be selectively removed from the reaction system, the conversion of C_2H_6 is no longer restricted by thermodynamic equilibrium, allowing the conversion rate of C_2H_6 to be increased at a lower temperature and developing active catalysts with high C_2H_4 selectivity and coking resistance.

Non-oxidative conversion of C_2H_6 to C_2H_4 is essentially a dehydrogenation process,[7] which could be achieved in an electrochemical process. Proton-conducting solid oxide electrolysers (SOEs) have been under the spotlight for their efficiency in converting electricity from renewable energy into fuels and chemicals.[8-10] They usually use ceramic components which therefore can deliver the advantages of durability and low production cost and the stack scale can be up to 100 kilowatt. Available exhaust heat stream in industry could add additional energy to the system with operation temperature at ~600-900°C. This temperature region well fit the operation conditions of the non-oxidative dehydrogenation process of C_2H_6 to C_2H_4. A recent study shows that the C_2H_6 conversion reaches a maximum of ~18% with traditional nickel-cermet anode and the coking formation is observed in the electrochemical dehydrogenation process.[11] As shown in **Figure 1**, C_2H_6 can be directly electrolyzed into C_2H_4 and H^+ ($C_2H_6 \rightarrow C_2H_4 + 2H^+ + 2e^-$) at anode, while the generated H^+ are transported through the electrolyte to cathode and form H_2 ($2H^+ + 2e^- \rightarrow H_2$), under an externally applied potential in proton-conducting SOEs. When CO_2 is fed into the cathode reacting with H^+ to produce CO ($CO_2 + 2H^+ + 2e^- \rightarrow CO + H_2O$), which would not only achieve the CO_2 reduction but also greatly improves the C_2H_6 dehydrogenation efficiency by decreasing the overpoentials between the two electrodes. This electrochemical non-oxidative dehydrogenation process of C_2H_6 into C_2H_4 would show huge application potential and the utilization of available waste industry heat flow would further improve electricity efficiency.

As the C-H bonds of C_2H_6 are more stable than the C-C bonds, electrochemical non-oxidative dehydrogenation of C_2H_6 to C_2H_4 in a proton-conducting SOE can selectively activate and break the C-H bonds of C_2H_6 in the porous electrode.[12,13] The electrochemical pumping of protons from C_2H_6 in anode is indeed a process of non-oxidative dehydrogenation under the electrochemical potentials. We use the proton-conducting barium zirconate cerate ($BaCe_{0.7}Zr_{0.1}Y_{0.1}Yb_{0.1}O_{3-\delta}$, BCZYYb) electrolyte which exhibits the proton conductivity as high as 6.2×10^{-3} S cm^{-1} with very small activation energy.[14,15] The high proton conductivity at low operation temperature and high flux would restrain the carbon coking from thermodynamic C_2H_6 splitting. Active metal-oxide interfaces can selectively activate C-H bonds while the electrochemical pumping of protons would constantly dehydrogenize C_2H_6 to form C_2H_4.[2,16-21] Active metal-oxide interfaces would therefore improve the coking resistance while the synergistic control of external applied voltage would further tailor the C_2H_6 cracking process leading to excellent catalysis durability. Electronic conductor $Nb_{1.33}Ti_{0.67}O_{4-\delta}$ is a typical redox-reversible ceramic electrode material,[22] and the doping of Mn in the lattice would create the oxygen vacancy to facilitate ionic conduction, which therefore offers a suitable scaffold to accommodate the metal-oxide interface for the electrochemical dehydrogenation of C_2H_6 in solid oxide electrolyser anode.

The typical metal catalysts including low-cost nickel and noble metal nanoparticles are generally used to construct strongly-interacting metal-oxide interfaces to facilitate the catalysis conversion of C_2H_6.[2,23-25] By using an impregnation method, traditional metal-oxide interfaces can be constructed on porous oxide scaffolds. However, the long-term instability of metal nanoparticles degrades catalysis performance, which is atrributed to the nanoparticle sintering and agglomerations at high temperatures.[26,27] In contrast, *in situ* growth of exsolved metal-oxide interfaces through a reversible phase decomposition under reducing conditions would be an alternative approach to enhance catalyst stability and activity.[28-30] The anchoring of metal nanoparticles on oxide particularly enhances stability and coking resistance, that is due the strong interactions in the exsolved metal-oxide interface structures at the nanoscale. Forming alloy particles at exsolved interface would be another way to increase coking resistance. The close interaction between different elements at atomic scale gives rise to the alloying effect which would be favourable to the catalysis activity and coking resistance for the C_2H_6 conversion to C_2H_4.[31] The Ni_xCu_{1-x} alloys would generate strong interfacial interactions in the interfacial architectures that are highly favorable for the C_2H_6 conversion to C_2H_4 in the porous electrode.

Here we present the electrochemical conversion of C_2H_6 to C_2H_4 in a non-oxidative dehydrogenation process in a proton-conducting SOE with the anode of Ni_xCu_{1-x}-doped $Nb_{1.33}(Ti_{0.8}Mn_{0.2})_{0.67}O_{4-\delta}$ (NTMO). Ni_xCu_{1-x} alloys nanoparticles are exsolved on NTMO backbone to grow embedded metal-oxide interface architecture. The strong interfacial interaction at exsolved metal-oxide interface would improve the stability and coking resistance at high temperature. We study the electrochemical pumping of protons from C_2H_6 for the directly non-oxidative dehydrogenation in the anode. We also investigate the electrochemical dehydrogenation of C_2H_6 in conjunction with CO_2 reduction in cathode and present the further enhanced C_2H_6 conversion.

EXPERIMENTAL SECTION

Experimet Prodecures. We synthesize five samples of the Cu-NTMO, $Ni_{0.25}Cu_{0.75}$-NTMO, $Ni_{0.5}Cu_{0.5}$-NTMO, $Ni_{0.75}Cu_{0.25}$-NTMO and Ni-NTMO using a microwave-assisted combustion method.[22] We denote the $NbTi_{0.4}Mn_{0.1}(Ni_xCu_{1-x})_{0.5}O_{4-\delta}$ as Ni_xCu_{1-x}-NTMO with x=0-1. We synthesize the $BaCe_{0.7}Zr_{0.1}Y_{0.1}Yb_{0.1}O_{3-\delta}$ (BCZYYb) powders using a liquid-phase combustion method.[14] We use X-ray diffraction (XRD; Miniflex 600, Japan) and X-ray photoelectron spectroscopy (XPS; ESCALAB 250Xi, USA) to investigate the oxidized and reduced samples. The cathode-supported half cells of NiO-BCZYYb|BCZYYb are fabricated by the co-pressing method, following by a sintering at 1450°C for 4 hours.[14] We prepare the electrode slurry composed of $NbTi_{0.4}Mn_{0.1}(Ni_xCu_{1-x})_{0.5}O_{4-\delta}$ and BCZYYb powders at a weight ratio of 65:35 with Ethyl cellulose additive to form porosity. Single cells (active area is 1 cm^2) are assembled with different anodes. We conduct the electrochemical tests of C_2H_6 dehydrogenation in the anode with 5% H_2/Ar (or CO_2) in the cathode at 700°C. We use an electrochemical workstation (Zahner IM6, Germany) to conduct the electrochemical measurements. We use a gas chromatograph (GC; Shimazu 2014, Japan) to analyse the product gas compositions. We observe the cathode microstructures using a scanning electron microscopy (SEM; SU-8010, Japan) and a high-resolution transmission electron microscopy (HRTEM; Tecnai F20, USA).

Theoretical Calculations. We conduct all the calculation of Density Functional Theory in the Vienna Ab Initio Simulation Package.[32] We use the generalized gradient approximation and we choose the Perdew-Burke-Ernzerhof (PBE) functional here to present the exchange correlation interactions.[33] We use the method of projector augmented wave (PAW) to investigate the interaction between core and valence electrons. The DFT-D3 method is implemented in VASP for the dispersion correction. The optimized rutile TiO_2 crystal with a 5×5×8 k-point grid gives a lattice parameter of 4.646 Å for *a* and *b* and 2.966 Å for *c*. We set an energy of 450 eV to the plane wave cut-off. We choose the periodic slab model by setting a p(4×2) superstructure with four Ti-O-Ti trilayers (48 Ti, 96 O) at (110) facet. We fix the bottom two Ti-O-Ti trilayers while we relax the top two trilayers. We set a thickness of 20 Å for the vacuum region. We sample the Brillouin zone by using a 3×3×1 k-point grid. We calculate the energy of oxygen vacancy formation of TiO_2 (110) surface according to $E_{for} = E_{def} - E_{perfect} - \mu_O$.[34] The E_{def}, $E_{perfect}$ and μ_O are the energy for a defective with a vacancy, the total energy of perfect surface and the energy of O atom taken from molecular O_2, respectively. We calculate the adsorption energy of C_2H_6 using $E_{ads} = E_{total} - E_{eth} - E_{slab}$. E_{total}, E_{slab} and E_{eth} are the energy of the adsorption system in total, the TiO_2 (110) system without adsorption and ethane molecule, respectively. The structures of six clusters (Ni11, Cu11, (Ni-Cu)-1, (Ni-Cu)-2, (Ni-Cu)-3, (Ni-Cu)-4) on TiO_2 (110) surface are constructed. We simulate the metal-oxide interface by setting a system composed of the Ni-Cu cluster on TiO_2 (110) with oxygen vacancy. We present the optimized configurations of the six clusters in **Figure S9**. We use the equation of $E_b = (E_{tot} - mE_{Cu} - nE_{Ni} - E_{slab})/(m + n)$ to study the binding energy (E_b) of the Ni/Cu atoms at surfaces. E_{tot}, E_{slab}, E_{Cu} and E_{Ni} are the energy of Ni/Cu atoms at surface in total, the surface, a Cu atom and a Ni atom, respectively. The m and n indicate the number of Cu and Ni atoms, respectively. We chose the (Ni-Cu)-4 structures for the subsequent calculation. The adsorption energy of C_2H_6 at interface is calculated according to the equation of $E_{ads} = E_{total} - E_{eth} - E_{slab*}$. E_{total}, E_{slab*}, and E_{eth} are the energy of the adsorption system in total, the TiO_2 (110) system with cluster adsorption and the ethane molecule, respectively. The structure after optimization and adsorption energy are shown in **Figure S10**. We conduct the transition state (TS) searches by the climbing image nudged elastic band (CI-NEB) method.[35]

RESULTS AND DISCUSSION

Figure 2a shows the XRD of the synthesized Ni_xCu_{1-x}-NTMO powder samples which indicates the homogeneous solid solutions with Ni/Cu dopant in lattice. We grow the exsolved Ni_xCu_{1-x}-NTMO interface by reducing the samples in 5%H_2/Ar. **Figure 2b** confirms the existence of Ni_xCu_{1-x} phase after reduction. XRD rietveld refinement patterns of the samples are presented in **Figure S1-S2**. XPS in **Figure S3** validates that Ni/Cu elements at at metallic state after reduction, confirming the exsolution of the Ni_xCu_{1-x} alloy from lattice. Thermo-gravimetric analysis (TGA) tests in **Figure S4** further confirm that the up to ~100% Ni/Cu metal are exsolved in this phase decomposition process while partial Mn^{4+} are reduced to Mn^{3+} to create the associated oxygen vacancies in lattice. **Figure 2c** gives the microstructure of $Ni_{0.5}Cu_{0.5}$-NTMO after reduction, showing the metal

particles uniformly embedding on oxide surface. The metal particles distribute in a very narrow range with a mean size of ~33 nm. **Figure 2d** presents the *in situ* grown $Ni_{0.5}Cu_{0.5}$-NTMO interface with metal particles deeply anchoring on NTMO backbone, which indicates a strong interaction at the exsolved interfaces. The anchoring interface architecture would not only prohibit the sintering of metal particles but also delivers enhanced resistance to carbon deposition from C_2H_6 conversion. Through a synergistic control of doping and non-stoichiometry, the exsolution of metal-oxide interface would be a universal method, which is expected to be extended to more metal-oxide interfaces on scaffolds.

The rutile Ni_xCu_{1-x}-NTMO oxides demonstrate a conductivity of ~30-150 S cm^{-1} (5% H_2/Ar atmosphere) and 1.5×10^{-5}~0.5 S cm^{-1} (air atmosphere) at ~400-800°C in **Figure S5**. **Figure S6** shows the observed oxygen exchange coefficient diagram of the samples. For the rutile scaffolds, the equilibrium time shows that the growth of exsolved metal-oxide interfaces effectively enhances the oxygen exchange process. With the intimate interaction between Ni and Cu in Ni_xCu_{1-x} alloy nanoparticles, the equilibrium time is further reduced by ~10-100 times, indicating the significant enhancement of oxygen exchange with the metal-oxide interfaces. These exsolved Ni_xCu_{1-x}-NTMO interfaces would facilitate the electrochemical dehydrogenation of C_2H_6 to C_2H_4 at external bias. A fully assembled cell consists of a dense 35 μm-thick BCZYYb electrolyte on a porous $Ni_{0.5}Cu_{0.5}$-NTMO anode, and a porous Ni-BCZYYb cathode in **Figure S7**. BCZYYb is an outstanding proton-conducting electrolyte with high ionic conductivity and proton transfer numbers at medium to high temperatures and we thus operate the electrochemical dehydrogenation of C_2H_6 at 700 °C. We conduct the non-oxidative dehydrogenation of C_2H_6 at anode while the simultaneous transportation of proton to the cathode and forming H_2 gas. Here we use external bias to promote C_2H_6 dehydrogenation process to generate C_2H_4 at anode. We pre-reduce the anode to exsolve the interface architectures consisting of metal nanoparticles are grown *in situ* and embedded in the NTMO backbones.

Figure 3a presents the dependence of current density on the applied voltages, confirming that the $Ni_{0.5}Cu_{0.5}$-NTMO anode enhances current density by approximately 100% in contrast to the Cu-NTMO anode. The growth of alloy nanoparticles greatly increases the current density to ~0.83 A cm^{-2} at 0.8 V with the optimal interface compositions in porous NTMO backbones. **Figure 3b** presents the dependence of current density on the exsolved interfaces, implying greatly improved C_2H_6 dehydrogenation with active interfaces. **Figure S8** demonstrates the lowest electrode polarization resistance of ~0.3 Ω cm^2 at 0.8 V with the $Ni_{0.5}Cu_{0.5}$-NTMO anode, indicating the significantly enhanced the electrode activity toward C_2H_6 conversion. The compositions of Ni_xCu_{1-x}-NTMO interface can further continuously engineer the catalysis activity of anodes with exsolved interface architectures. And the optimum composition of $Ni_{0.5}Cu_{0.5}$-NTMO is observed to deliver the highest electrode acitvity. **Figure 3c** shows the summarized data of the electrode polarization resistances of the non-oxidative dehydrogenation of C_2H_6 with different interface compositions at 0.4-0.8 V at 700°C. The results show that the decrease of electrode polarization resistance is closely related to the synergistic control of interface compositions and applied voltages. We further conduct theoretical calculation of transition states to understand the dehydrogenation of C_2H_6 to C_2H_4 at metal-oxide interface. **Figure S9** shows the interface models with different configurations in which we simulate the metal-oxide interface with different metal clusters stacked on defected TiO_2 surface. **Figure S10** shows the adsorption configurations of C_2H_6 at the surface of defected TiO_2 and the metal-oxide interface, which clearly confirms the enhanced chemical adsorption with interface interactions in contrast to defected surfaces. **Figure 3d** presents that the energy barrier is 0.91 eV and 0.40 eV for the dehydrogenation of C_2H_6 at $NiCu/TiO_2$ interface, which is much lower than those at Ni/TiO_2 and Cu/TiO_2 interface, indicating that the coupling between defected surface and metal alloy clusters is beneficial to the dehydrogenation progress. We present the calculated transition states of the dehydrogenation progress at Ni/TiO_2 and Cu/TiO_2 in **Figure S11**. The metal-oxide interfaces architecture is expected to highly facilitate the dehydrogenation process while the alloying effects wold further enhance the catalysis activity, which well fits our observed experimental results.

Figure 4a presents the anode product analysis during the electrochemical non-oxidative dehydrogenation of C_2H_6 with different Ni_xCu_{1-x} compositions while the protons are ionically pumped to the cathodes. Here 100% concentration of C_2H_6 is supplied to the anode for electrochemical measurements. We study the thermal cracking of C_2H_6 under open circuit conditions and we confirm 30.5% of C_2H_6 conversion in **Figure S12**. When a voltage is applied, C_2H_4 concentrations positively depend on applied potential, which indicates that C_2H_6 can be

successfully converted to C_2H_4 by this electrochemical method even though there still exists some H_2 and a small amount of CH_4 in anode. The C_2H_6 conversion reaches 66.3% with C_2H_4 selectivity of 99.7% in **Figure 4b** at 0.8 V, which is the best C_2H_6 conversion and C_2H_4 selectivity in contrast to the reported C_2H_6 conversion both in oxidative and non-oxidative processes. It is observed that the exsolved interfaces increase the C_2H_4 production by about 35~50%, which indicates the favourable cleavage of C-H bonds at interfaces. The dehydrogenation process is thus controlled by the synergy of external voltage and interface compositions at anode. **Figure 4c** shows the electrochemical pumping of protons from the anode to the cathode and form H_2, while the amount of H_2 depends on the current. The $Ni_{0.5}Cu_{0.5}$-NTMO anode gives 0.83 A cm^{-2} at 0.8 V, that ~6.3% H_2 is generated in the cathode. The electrochemical performance is significantly enhanced by using ceramic $Ni_{0.5}Cu_{0.5}$-NTMO electrode with exsolved metal-oxide interfaces, while the C_2H_6 conversion together with C_2H_4 yields and selectivity are therefore remarkably improved in contrast to the nickel-cermet anode.[11]

The electrochemical dehydrogenation of C_2H_6 leads to the generation of C_2H_4 in anode while thermal splitting of C_2H_6 to C_2H_4 is also present in anode. We observe ~100% of Faraday efficiency for the generation of H_2 in cathode for electrochemical C_2H_6 dehydrogenation as shown in **Figure S13a**. The Faraday efficiency is ~100% for C_2H_4 production in the process of electrochemical dehydrogenation of C_2H_6 in **Figure S13c**. The extra C_2H_4 in anode is from thermal splitting of C_2H_6 which could be considered as background even though some fluctuations may be present in different processes. In control experiments, we supply a mixture of H_2/C_2H_6 with the ratio in the range of 0-10 to anode for the thermal splitting tests under open circuit conditions. We observe that the C_2H_6 conversion only reaches 30.5% with the H_2/C_2H_6 ratio at 0, which is far below the theoretical conversion of 70.0%. It is observed that higher H_2 content leads to lower C_2H_6 conversion for the H_2/C_2H_6 ratio ranging from 0 to 10. At the H_2/C_2H_6 ratio of 10, the C_2H_6 conversion is significantly decreased to 10.2%, which is remarkably lower than the theoretical C_2H_6 conversion of 51.5%. The presence of H_2 with concentration in a wide range in anode significantly changes the C_2H_6 conversion in thermal splitting process. In contrast, we supply a mixture of H_2/C_2H_6 with the ratio in the range of 0-10 to anode for the electrochemical dehydrogenation tests. As shown in **Figure S14**, the C_2H_6 conversion is as high as 66.3% at H_2/C_2H_6 ratio of 0, which is comparable to the theoretical C_2H_6 conversion of 70.0% and significantly higher than the observed C_2H_6 conversion of 30.5% in thermal splitting tests under open circuit conditions. The enhancement of C_2H_6 conversion confirms the dominance of electrochemical C_2H_6 conversion. At the H_2/C_2H_6 ratio of 10, the C_2H_6 conversion still maintains a value of as high as 61.6%, which further confirms the dominance of electrochemical C_2H_6 conversion even in a gas mixture with initial C_2H_6 content lower than 10%. The electrochemical pumping of proton from C_2H_6 gives rise to the enhanced C_2H_6 conversion even with a significantly high content of hydrogen. It should be noted that the conversion of 100%C_2H_6 can reach 75.2% in anode in the electrochemical dehydrogenation process if combined with CO_2 reduction in cathode as discussed later, which is much higher than the 70.0% conversion as calculated from the thermodynamic equilibrium in thermal splitting.

Figure 4d presents the operation of the non-oxidative dehydrogenation of C_2H_6 with the $Ni_{0.5}Cu_{0.5}$-NTMO anode in a proton-conducting SOE, which indicates remarkable stability after 10 hours at 700°C and 0.6 V. The current density and C_2H_4 generation remain stable during the operation. Exsolved interface architectures lead to enhanced stability by preventing nanoparticles from coalescing due to a decrease in surface energy. This strong interfacial interaction would also give rise to improved charge transfer and coking resistance at high temperatures. We isolate a single nanoparticle anchored on NTMO scaffold after tests. As shown in **Figure S15**, the nanoparticle is deeply anchored on the NTMO substrate while Cu and Ni are homogeneously distributed in the particle, revealing the homogeneous alloying features of the metal nanoparticles. The microstructure of the $Ni_{0.5}Cu_{0.5}$-NTMO anode generally remains unchanged after stability test. In addition, no coking formation is visually observed in $Ni_{0.5}Cu_{0.5}$-NTMO anode after stability test for electrochemical dehydrogenation of C_2H_6. As shown in **Figure S16**, the chemical state of Mn, Ni and Cu remain basically unchanged before and after stability test. The microstructure of the porous $Ni_{0.5}Cu_{0.5}$-NTMO anode maintains well after stability test. The embedding effect would provide improved high temperature stability against the severe long-term agglomeration and carbon deposition from C_2H_6 conversion.

In our work, the deep cracking of ethane would lead to carbon formation on electrodes. We exsolve metal-oxide interface architectures and add copper to nickel to form alloying effects to enhance coking resistance. One reason

would be the the strong interactions at the exsolved interfaces that enhances coking resistance. The other would be the alloying effects with strong interactions between different elements that can further enhance the resistance to carbon deposition. It is well known that the C formed during the dehydrogenation of ethane results from the deep cracking of ethane. We simplify the oxide as defected TiO_2 and then construct a model of metal-oxide interfaces. **Figure S17** presents the Gibbs free energy of the ethane deep cracking process calculated from the reaction equation as follows:

$$C_2H_6\ (g) + 2^* = 2C^* + 3H_2\ (g)$$

Where "C*" is C atom adsorbed on cluster/TiO_2 system. And "*" provides active position. C_2H_6 (g) and H_2 (g) means that ethane and hydrogen are in gaseous state. The Gibbs free energy is calculated by:

$$\Delta G = \Delta E + \Delta ZPE - T\Delta S$$

Where ΔE is the energy calculated by DFT; ΔZPE is the zero-point energy; T is the temperature; ΔS is the Entropy. The Gibbs free energy of the progress is 0.306 eV on Ni/TiO_2 system which is much lower than the 3.24 eV on Cu/TiO_2 system. It should be noted that the Gibbs free energy of the progress is enhanced to 2.45 eV on (Ni-Cu)/TiO_2 system. It suggests that it might be not a difficult process for the ethane deep cracking on Ni/TiO_2 system but the alloy effectively increases the energy barrier and therefore significantly enhances the coking resistance for the ethane dehydrogenation process.

This electrochemical process includes the C_2H_6 conversion in anode and the ionically pumping protons from anode to cathode. **Figure 5a** shows the electrochemical performance of CO_2 reduction in cathode in combination with C_2H_6 dehydrogenation in anode at the same time. The exsolved interface architectures in porous anode backbones enhance the performances with the optimum interface composition of $Ni_{0.5}Cu_{0.5}$-NTMO observed. Similar changing trend is also observed for short-term performance and *in situ* impedance in **Figure S18-S19**. **Figure 5b** shows the H_2/CO ratio *versus* interface compositions and external voltages, which displays that the higher external bias promote CO_2 reacting with H^+ while best composition is the $Ni_{0.5}Cu_{0.5}$-NTMO composite with appropriate interface composition in anode. We conduct a control experiment by directly pumping the gas mixture of H_2/CO_2 to cathode under open circuit conditions, where the supplied H_2 is identical to the H_2 generation amount in cathode during electrochemical C_2H_6 dehydrogenation as shown in **Figure S20a**. The ratio of CO/H_2 is generally at ~99:1 calculated from the thermodynamic equilibrium of reverse waster gas shift reaction as shown in Figure **S20b**. In addition, the observed ratio of CO/H_2 in control experiment is only ~20:1, which indicates that the CO generation is far below the thermodynamic equilibrium of reverse gas shift reaction under open circuit conditions. In the electrochemical process, the observed ratio of CO/H_2 is enhanced to as high as ~80:1, which implies that the electrochemical reduction of CO_2 to CO may be a dominant reaction even though the reverse water shift gas reaction is still present.

Figure 5c shows the conversion of C_2H_6 to chemicals at anode and CO_2 reduction is simultaneously performed at cathode. The C_2H_4 selectivity of 99.9% while the C_2H_6 conversion reaches 75.2% in the $Ni_{0.5}Cu_{0.5}$-NTMO anode at ambient pressure and 0.8 V as shown in **Figure 5c and Figure S21a**. This higher performance of integrating CO_2 reduction in cathode with electrochemical dehydrogenation of C_2H_6 in cathode would be attributed to the reduced electrochemical potential between the two electrodes that greatly improves the dehydrogenation process of C_2H_6 in anode. We also observe ~100% of Faraday efficiency for CO/H_2 in cathode for electrochemical dehydrogenation of C_2H_6 in conjunction with CO_2 reduction in cathode as shown in **Figure S13b**. The Faraday efficiency is ~100% for C_2H_4 production in the process of electrochemical dehydrogenation of C_2H_6 with CO_2 reduction in **Figure S13d**. The conversion of 100%C_2H_6 can reach ~75.2% in anode in the electrochemical dehydrogenation process combined with CO_2 reduction in cathode by decreasing the overpoentials between the two electrodes, which is much higher than the ~70.0% conversion calculated from the thermodynamic equilibrium in thermal splitting under operation conditions. **Figure S21b** presents the operation of the non-oxidative dehydrogenation of C_2H_6 for 10 hours, which further validates the stability even with CO_2 reduction in cathode. In **Figure 5d**, we can find the clear structures of the porous $Ni_{0.5}Cu_{0.5}$-NTMO electrode which well adheres to the BCZYYb electrolyte, indicating a compatibility between electrode and electrolyte after electrochemical test. The $Ni_{0.5}Cu_{0.5}$ particles remain basically unchanged without obvious carbon deposition, which indicates resistance to agglomeration, sintering and carbon deposition of the interface architectures.

CONCLUSION

In summary, we show an alternative approach to electrochemically convert C_2H_6 to C_2H_4 with high C_2H_6 conversion, high C_2H_4 selectivity in a proton-conducting solid oxide electrolyser. We *in situ* exsolve metal-oxide interface architectures at nanoscale delivers strong interface interactions, which enhances the C-H bonds activation, sintering stability and coking resistance. Electrochemical non-oxidative dehydrogenation of C_2H_6 in anode in combination with CO_2 reduction in cathode shows the enhanced C_2H_6 conversion of 75.2% with ~100% C_2H_4 selectivity. The electrochemical pumping of hydrogen ions at metal-oxide interfaces facilitates the exceptionally high anode activity while the interface compositions further engineer the ethane conversion. The porous anode backbone with *in situ* grown metal-oxide interfaces at nanoscale displays significantly improved catalyst stability and coking resistance. This work would not only provide an efficient and reliable electrochemical process for C_2H_6 conversion but also offer an alternative in wealth of other alkane conversion into worthy chemicals.

ASSOCIATED CONTENT

Supporting Information: XRD refinement of Ni_xCu_{1-x}-NTMO, XPS of element states in Ni_xCu_{1-x}-NTMO, TGA of phase decomposition, Mixed conductivity of Ni_xCu_{1-x}-NTMO, Conductivity relaxation of Ni_xCu_{1-x}-NTMO, SEM of cell microstructure, DFT calculation of ethane deep cracking at interface, Control experiments and electrochemical measurements in Supporting Information are available free of charge on the ACS Publications website.

AUTHOR INFORMATION

Corresponding Author

*E-mail: kxie@fjirsm.ac.cn.

ORCID

Kui Xie: 0000-0002-1215-0271

Author Contributions

X.Z. and L.Y. contributed equally to this work. H.L. conducted the first principle calculations. K.X. supervised this work. All authors were involved in the data analysis and discussion. Correspondence and materials request should be addressed to K.X. (kxie@fjism.ac.cn)

Notes

The authors declare no competing financial interest.

ACKNOWLEDGMENTS

We acknowledge the National Key Research and Development Program of China (2017YFA0700102), the Natural Science Foundation of China (91845202), the Strategic Priority Research Program of the Chinese Academy of Sciences (XDB2000000), Natural Science Foundation of Fujian Province (2018J01088) and the US National Science Foundation (DMR-1832809) for funding this work.

REFERENCES

(1) Melikoglu, M.; Shale gas: Analysis of its Role in the Global Energy Market. *Renew. Sust. Energ. Rev.* **2014**, 37, 460-468.
(2) Sattler, J.; Ruiz-Martinez, J.; Santillan-Jimenez, E.; Weckhuysen, M.; Catalytic Dehydrogenation of Light Alkanes on Metals and Metal Oxides. *Chem. Rev.* **2014**, 114, 10613-10653.
(3) Stangland, E. E.; Shale Gas Implications for C_2–C_3 Olefin Production: Incumbent and Future Technology. *Annu. Rev. Chem. Biomol.* **2018**, 9, 341-364.
(4) Xiang, Y.; Wang, H.; Cheng, J.; Matsubu, J.; Progress and Prospects in Catalytic Ethane Aromatization. *Catal. Sci. Technol.* **2018**, 8, 1500-1516.
(5) Song, Y.; Lin, L.; Feng, W.; Zhang, X.; Dong, Q.; Li, X.; Lv, H.; Liu, Q.; Yang, F.; Liu, Z.; Wang, X.; Bao, X.; Interfacial Enhancement by gamma-Al_2O_3 of Electrochemical Oxidative Dehydrogenation of Ethane to Ethylene in Solid Oxide Electrolysis Cells. *Angew. Chem.-Int. Edit.* **2019**, 58, 16043-16046.
(6) Venegas, J. M.; McDermott, W. P.; Hermans, I.; Serendipity in Catalysis Research: Boron-Based Materials for Alkane Oxidative Dehydrogenation. *Acc. Chem. Res.* **2018**, 51, 2556-2564.
(7) Wang, L.; Zhang, Y.; Xu, J.; Diao, W.; Karakalos, S.; Liu, B.; Song, X.; Wu, W.; He, T.; Ding, D.; Non-oxidative Dehydrogenation of Ethane to Ethylene over ZSM-5 Zeolite Supported Iron Catalysts. *Appl. Catal. B-Environ.* **2019**, 256, 117816.
(8) Song, Y.; Zhou, S.; Dong, Q.; Li, Y.; Zhang, X.; Ta, N.; Liu, Z.; Zhao, J.; Yang, F.; Wang, G.; Bao, X.; Oxygen Evolution Reaction over the Au/YSZ Interface at High Temperature. *Angew. Chem.-Int. Edit.* **2019**, 58, 4617-4621.
(9) Li, Y.; Li, Y.; Wan, Y.; Xie, Y.; Zhu, J.; Pan, H.; Zheng, X.; Xia, C.; Perovskite Oxyfluoride Electrode Enabling Direct Electrolyzing Carbon Dioxide with Excellent Electrochemical Performances. *Adv. Energy Mater.* **2019**, 9, 1803156.
(10) Yu, J.; He, Q.; Yang, G.; Zhou, W.; Shao Z.; Ni, M.; Recent Advances and Prospective in Ruthenium-Based Materials for Electrochemical Water Splitting. *ACS Catal.* **2019**, 9, 9973-10011.
(11) Ding, D.; Zhang, Y.; Wu, W.; Chen, D.; Liu, M.; He, T.; A Novel Low-Thermal-Budget Approach for the Co-Production of Ethylene and Hydrogen via the Electrochemical Non-Oxidative Deprotonation of Ethane. *Energy Environ. Sci.* **2018**, 11, 1710-1716.
(12) Bian, Y., Kim, M., Li, T., Asthagiri, A.; Weaver, J. F.; Facile Dehydrogenation of Ethane on the IrO_2 (110) Surface. *J. Am. Chem. Soc.* **2018**, 140, 2665-2672.
(13) Huang, R.; Zhang, B.; Wang, J.; Wu, K.; Shi, W.; Zhang, Y.; Liu, Y.; Zheng, A.; Schloegl, R.; Su, D.; Direct Insight into Ethane Oxidative Dehydrogenation over Boron Nitrides. *Chemcatchem* **2017**, 9, 3293-3297.
(14) Yang, L.; Wang, S.; Blinn, K.; Liu, M.; Liu, Z.; Cheng, Z.; Liu, M.; Enhanced Sulfur and Coking Tolerance of a Mixed Ion Conductor for SOFCs: $BaZr_{0.1}Ce_{0.7}Y_{0.2-x}Yb_xO_{3-\delta}$. *Science* **2009**, 326, 126-129.
(15) Chen, Y.; Bu, Y.; Zhang, Y.; Yan, R.; Ding, D.; Zhao, B.; Yoo, S. Y.; Dang, D.; Hu, R.; Yang, C.;. Liu, M.; A Highly Efficient and Robust Nanofiber Cathode for Solid Oxide Fuel Cells. *Adv. Energy Mater.* **2017**, 7, 1601890.
(16) Xiong, H., Lin, S., Goetze, J., Pletcher, P. D.; Datye, A. K.; Thermally Stable and Regenerable Pt-Sn Clusters for Propane Dehydrogenation Prepared via Atom Trapping on Ceria. *Angew. Chem.-Int. Edit.* **2017**, 56, 8986-8991.
(17) Jiao, F.; Pan, X.; Gong, K.; Chen, Y.; Li, G.; Bao, X.; Shape-Selective Zeolites Promote Ethylene Formation from Syngas via a Ketene Intermediate. *Angew. Chem.-Int. Edit.* **2018**, 57, 4692-4696.
(18) Schreiber, M. W.; Plaisance, C. P.; Baumgärtl, M.; Reuter, K.; Lercher, J. A.; Lewis-Brønsted Acid Pairs in Ga/H-ZSM-5 to Catalyze Dehydrogenation of Light Alkanes. *J. Am. Chem. Soc.* **2018**, 140, 4849-4859.
(19) Schwach, P.; Pan, X.; Bao, X.; Direct Conversion of Methane to Value-Added Chemicals over Heterogeneous Catalysts: Challenges and Prospects. *Chem. Rev.* **2017**, 117, 8497-8520.
(20) Zhang, Z.; Wang, S.; Song, R.; Cao, T.; Luo, L.; Chen, X.; Gao, Y.; Lu, J.; Li, W.; Huang, W.; The Most Active Cu Facet for Low-Temperature Water Gas Shift Reaction. *Nat. Commun.* **2017**, 8, 488.
(21) Chen, Y.; Glee, B.; Tang, Y.; Wang, Z.; Zhao, B.; Wei, Y.; Zhang, L.; Yoo, S.; Pei, K.; Kim, J. H.; Ding, Y.; Hu, P.; Tao, F.; Liu, M.; A Robust Fuel Cell Operated on Nearly Dry Methane at 500 Degrees C Enabled by

Synergistic Thermal Catalysis and Electrocatalysis. *Nat. Energy* **2018**, 3, 1042-1050.

(22) Li, S.; Qin, Q.; Xie, K.; Wang, Y.; Wu, Y.; High-Performance Fuel Electrodes Based on $NbTi_{0.5}M_{0.5}O_4$ (M = Ni, Cu) with Reversible Exsolution of the Nano-Catalyst for Steam Electrolysis. *J. Mater. Chem. A* **2013**, 1, 8984-8993.

(23) Huang, W.; Sun, G.; Tian, C.; Surface Chemistry of Group IB Metals and Related Oxides. *Chem. Soc. Rev.* **2017**, 46, 1977-2000.

(24) Polo-Garzon, F.; Bao, Z.; Zhang, X.; Huang, W.; Wu, Z.; Surface Reconstructions of Metal Oxides and the Consequences on Catalytic Chemistry. *ACS Catalysis* **2019**, 9, 5692-5707.

(25) Hua, Q.; Cao, T.; Gu, X.; Lu, J.; Jiang, Z.; Pan, X.; Luo, L.; Li, W.; Huang, W.; Crystal-Plane-Controlled Selectivity of Cu_2O Catalysts in Propylene Oxidation with Molecular Oxygen. *Angew. Chem.-Int. Edit.* **2014**, 53, 4856-4861.

(26) Zhou, Y.; Zhou, Z.; Song, Y.; Zhang, X.; Guan, F.; Lv, H.; Liu, Q.; Miao, S.; Wang, G.; Bao, X.; Enhancing CO_2 Electrolysis Performance with Vanadium-doped Perovskite Cathode in Solid Oxide Electrolysis Cell. *Nano Energy* **2018**, 50, 43-51.

(27) Schmies, H.; Bergmann, A.; Drnec, J.; Wang, G.; Teschner, D.; Kuhl, S.; Sandbeck, D. J. S.; Cherevko, S.; Gocyla, M.; Shviro, M.; Heggen, M.; Ramani, V.; Dunin-Borkowski, R. E.; Mayrhofer, K. J. J.; Strasser, P.; Unravelling Degradation Pathways of Oxide-Supported Pt Fuel Cell Nanocatalysts under *In Situ* Operating Conditions. *Adv. Energy Mater.* **2018**, 8, 1701663.

(28) Ye, L.; Zhang, M.; Huang, P.; Guo, G.; Hong, M.; Li, C.; Irvine, J. T. S.; Xie, K.; Enhancing CO_2 Electrolysis through Synergistic Control of Non-stoichiometry and Doping to Tune Cathode Surface Structures. *Nat. Commun.* **2017**, 8, 14785.

(29) Wang, W.; Gan, L.; Lemmon, J. P.; Chen, F.; Irvine; J. T. S.; Xie, K.; Enhanced Carbon Dioxide Electrolysis at Redox Manipulated Interfaces. *Nat. Commun.* **2019**, 10, 1550.

(30) Irvine, J. T. S.; Neagu, D.; Verbraeken, M. C.; Chatzichristodoulou, C.; Graves, C.; Mogensen, M. B.; Evolution of the Electrochemical Interface in High-Temperature Fuel Cells and Electrolysers. *Nat. Energy* **2016**, 1, 15014.

(31) Lu, J.; Zhu, C.; Pan, C.; Lin, W.; Lemmon, J. P.; Chen, F.; Li, C.; Xie, K.; Highly Efficient Electrochemical Reforming of CH_4/CO_2 in a Solid Oxide Electrolyser. *Sci. Adv.* **2018**, 4, eaar5100.

(32) Kresse, G.; Furthmuller, J.; Efficiency of Ab-Initio Total Energy Calculations for Metals and Semiconductors Using a Plane-Wave Basis Set. *Comp. Mater. Sci.* **1996**, 6, 15-50.

(33) Perdew, J. P.; Burke, K.; Ernzerhof, M.; Generalized Gradient Approximation Made Simple. *Phys. Rev. Lett.* **1996**, 77, 3865-3868.

(34) Cheng, F.; Lin, G.; Hu, X.; Xi, S.; Xie, K.; Porous Single-Crystalline Titanium Dioxide at 2 cm Scale Delivering Enhanced Photoelectrochemical Performance. *Nat. Commun.* **2019**, 10, 3618.

(35) Henkelman, G.; Uberuaga, B. P.; Jonsson, H.; A Climbing Image Nudged Elastic Band Method for Finding Saddle Points and Minimum Energy Paths. *J. Chem. Phys.* **2000**, 113, 9901-9904.

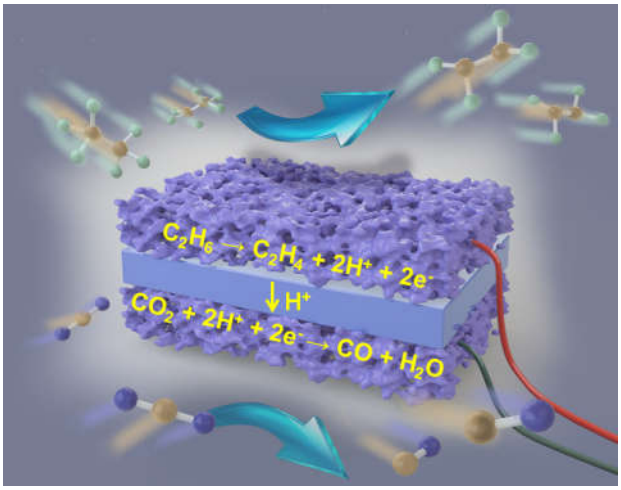

Figure 1. Here the C_2H_6 is converted to C_2H_4 in anode and H^+ in anode while CO_2 is reacting with H^+ to generate CO and H_2O in cathode in a simultaneous process in a proton-conducting solid oxide electrolyser.

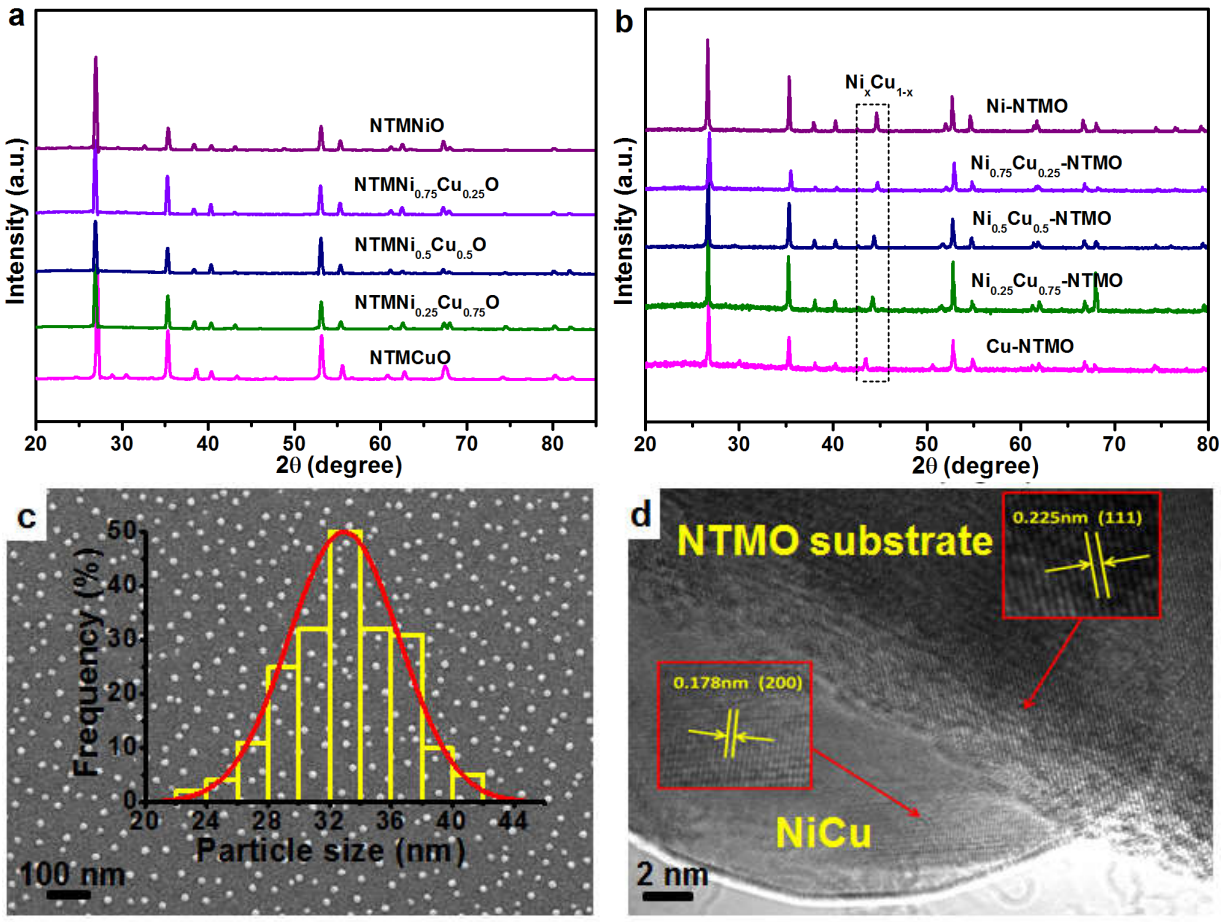

Figure 2. XRD of (**a**) oxidized samples, (**b**) reduced samples; (**c**) SEM image of the reduced $Ni_{0.5}Cu_{0.5}$-NTMO; (**d**) HRTEM microscopic result of the reduced $Ni_{0.5}Cu_{0.5}$-NTMO.

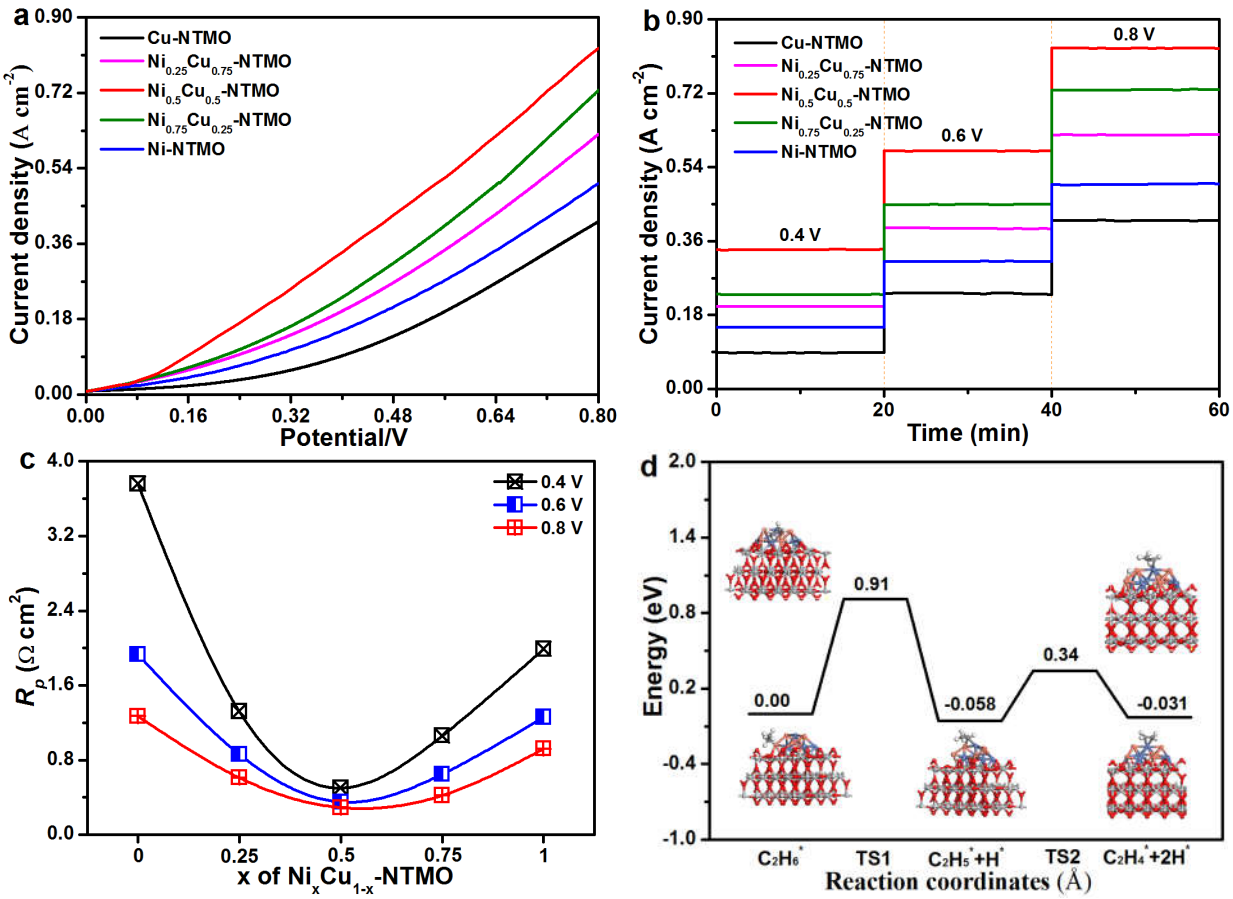

Figure 3. (**a**) The current–voltage (*I–V*) curves of the solid oxide electrolysers with different anodes for C_2H_6 dehydrogenation at 700°C; (**b**) The short-term operation of C_2H_6 dehydrogenation with the composite anodes at different voltages; (**c**) The electrode polarizations with different anodes at 0.4-0.8 V at 700°C; (**d**) Potential energy profile for the ethane dehydrogenation on $NiCu/TiO_2$ interface. (carbon in gray, copper in orange, nickel in bule, titanium in silver white, oxygen in red and hydrogen in white)

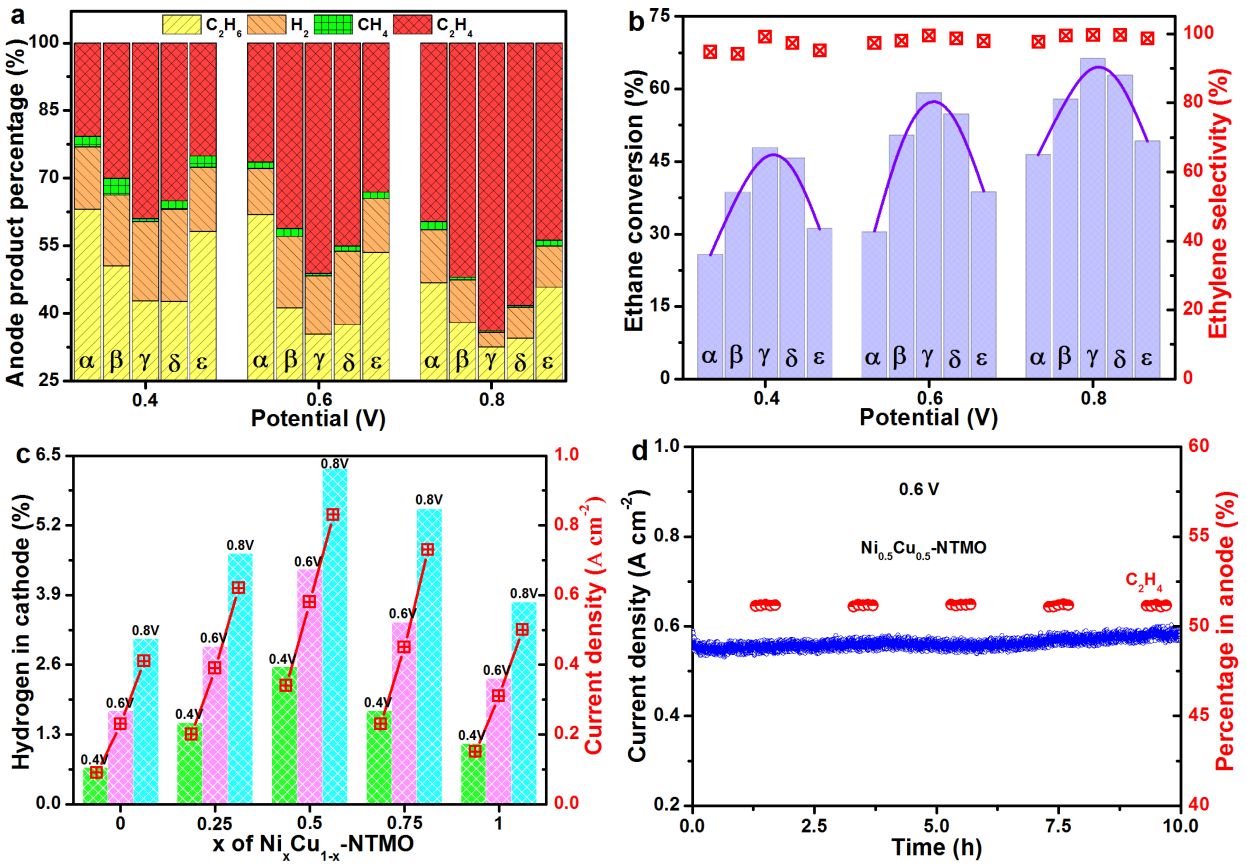

Figure 4. (**a**) The product analysis of electrochemical dehydrogenation of C_2H_6 with different anodes; (**b**) C_2H_6 conversion and C_2H_4 selectivity; (**c**) The amount of H_2 depends on the current in the cathode; (**d**) The short term performance of the electrochemical dehydrogenation of C_2H_6 with the $Ni_{0.5}Cu_{0.5}$-NTMO anode in a proton-conducting SOE. (α: Cu-NTMO, β: $Ni_{0.25}Cu_{0.75}$-NTMO, γ: $Ni_{0.5}Cu_{0.5}$-NTMO, δ: $Ni_{0.75}Cu_{0.25}$-NTMO, ε: Ni-NTMO)

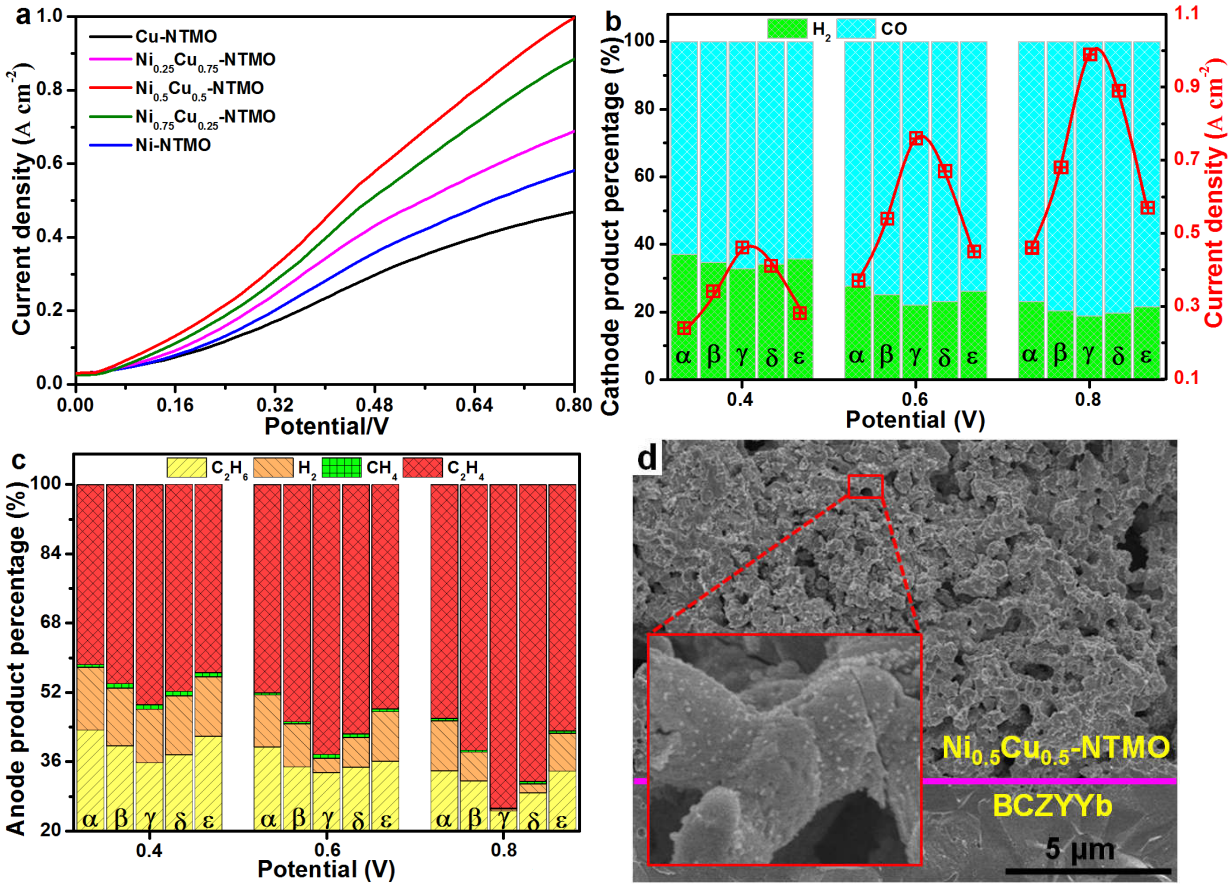

Figure 5. (**a**) The current–voltage (*I–V*) relationship of CO_2 electrolysis with C_2H_6 conversion at 700°C; (**b**) Cathode product analysis at various voltages; (**c**) The product analysis in the anode; (**d**) SEM images of the $Ni_{0.5}Cu_{0.5}$-NTMO porous electrodes after electrochemical test. (α: Cu-NTMO, β: $Ni_{0.25}Cu_{0.75}$-NTMO, γ: $Ni_{0.5}Cu_{0.5}$-NTMO, δ: $Ni_{0.75}Cu_{0.25}$-NTMO, ε: Ni-NTMO)